Noise Correlations Measurements for extended models using tensor networks

Kerman Gallego Lizarribar

Supervised by: Dr. Javier Argüello Luengo

Departament de Física, Universitat Politecnica de Catalunya, Campus Nord B4-B5, 08034 Barcelona, Spain
16 August 2024

Spontaneously symmetry-broken (SSB) phases are locally ordered states of matter. Because of their specific ordering, their presence is usually witnessed by means of local order parameters. In this Thesis, we investigate different characterization schemes that allows one to detect spontaneously broken symmetries in cold atom experiments where single-site imaging of optical lattices is not accessible. For that, we characterize several detection methods, including time-of-flight measurements and noise correlation measurements. Using tensor network methods, we first motivate our approach on a Bose-Hubbard model, where the salient physics is be presented. Later on, we benchmark our approach on an extended Fermi-Hubbard model, where the final protocol is presented. Our numerical analysis shows that noise correlations can accurately capture the presence of spontaneously broken symmetries, thus representing an alternative and powerful strategy to characterize strongly interacting quantum matter.

Keywords: Tensor Networks, quantum phases, noise-correlation measurements, cold atoms

Acknowledgements

I would like to thank Luca Barbiero and Maciej Lewenstein for the theoretical proposals, Christof Weitenberg for the experimental suggestions, and my supervisor for the provided help in the academic world, not only from the scientific point of view. I also acknowledge the Catalonia Quantum Academy (CQA).

Kerman Gallego Lizarribar: kgalleli40@alumnes.ub.edu

Contents

1 Introduction

In condensed matter physics, correlations and fluctuations of quantum many-body systems lead to exciting phenomena that do not have a classical counterpart [DDM+23]. Some examples are high-temperature superconductors [BM86], quantum spin liquids [DS13], and the fractional quantum Hall effect [Lau83].

To understand the microscopic origin of such phenomena, one common approach is to propose a simplified Hamiltonian that replicates the interactions responsible for these properties. One of this toy models, for example, is the Hubbard model for high T_c superconductors [GK63].

Hubbard models consist of quantum particles, either bosons or fermions, arranged in a lattice, which are characterized by the competition between non-commuting terms. The first is the tunneling, equivalent to the kinetic term in the Schrödinger equation, which favors the delocalization of the particles. Subsequently, interactions are incorporated into the system. For the simplest models local interactions are considered, while long-range interactions can be introduced to find even more exotic phenomena. These additions result in a many-body Hamiltonian that is difficult to solve numerically and requires different strategies to tackle them.

In the early 80s, Feynman proposed to use quantum systems as computers with the goal of understanding quantum systems themselves [Fey82]. In recent years, this idea has been further developed, and early prototypes of digital quantum computers are becoming available.

As this technological revolution occurs, platforms, such as ultracold atomic gases in optical lattices have proven to offer experimental benchmarks for condensed matter models [LSA+07] [GB17]. This is the idea behind analog simulation: mimicking the physics of interest by a highly controllable quantum system, where precise measurement techniques provide information about it. In general, this characterization is achieved by order parameters, i.e., expectation values of some operators. The problem with such platforms is that not all observables are easily accessible.

In the case of atoms trapped in the effective optical lattice induced by a retrorreflected beam, contact forces induce local interactions. Together with the tunneling to neighbor sites, this provides an immediate realization of a hubbard model. In addition, recent experimental progress in atomic gas microscopy has allowed a real space imaging of the occupation of each lattices site, offering an easy detection of phases where atoms are highly localized.

Nevertheless, the addition of nearest neighbor interactions is not straightforward. A feasible solution is using dipolar atoms in subwavelength lattices [SDS+23]. Their dipolar interaction is however weak and, in order to achieve nearest-neighbor interactions that compete with the tunneling rate, one needs to use short lattice spacings (in the order of 200 nm). The challenge is that atoms are now at subwavelength distances, and the diffraction limit does not allow for spatial resolution using visible light. In such cases, time-of-flight measurements can be carried out [GME+02], leaving atoms in free expansion for a given time. In this way, the particles are more distant from each other at the imaging stage, enabling a real space measurement. Interestingly, after this ballistic expansion, the detected position of the atom is related to initial momentum it had in the lattice, which allows one to access the atomic configuration in reciprocal space. Even if convenient for states with a narrow momentum distribution, characterization of localized states become less accessible.

Measuring the correlations between different momenta (noise correlation measurements)

can provide further information about the system, but this is not always sufficient for its complete understanding. Thus, protocols that exploit such measurements as much as possible are needed to make quantum simulators practical when single-site imaging is not accessible [ADL04]. In this work, we will propose different strategies to distinguish among different quantum phases using these correlations of noise, as we will test them with numerical simulations, predicting experimental outcomes and checking their usefulness.

To choose the appropriate numerical method, several points have to be considered. Firstly, quantum phase transitions appear in the thermodynamic limit, so large-scale numerical simulations are needed. This is the biggest handicap of exact diagonalization, as the current computing power and memory are far from sufficient, due to the exponential growth of the Hilbert space with the number of atoms involved in the calculation. In some cases, these simulations can be carried out using quantum Monte Carlo methods, but this is challenged in the case of fermionic and geometrically frustrated systems due to the 'minus-sign problem' [dS03]. Mean field theory can capture the behavior of the thermodynamic limit, but it does not account for quantum correlations [ANB77].

A good candidate that circumvents the previous weaknesses is tensor networks: an economical ansatz for many-body systems with local entanglement. Its limitations are the amount and structure of entropy in the quantum many-body state, but not system size or type of particle. Those, however, are not a problem for ground states of gapped Hamiltonians with low dimensionality, making these methods highly suitable for studying such systems [Sch11]. It should be noted, though, that many other problems in nature do not meet these conditions, so their usefulness is highly limited. This is where quantum simulators, once fully developed and practical, are expected to outperform.

Thus, the main goal of this project is to use such tensor network methods to test a new procedure proposed for the detection of some phases in quantum simulators, improving their versatility. For this purpose, in Section 2 we will start by analyzing bosonic models, developing a strong intuition about the momentum distribution of both, localized and delocalized states. In Section 3, we will study fermionic models, understanding the limitations of the experimental setups to detect some localized phases. Finally, we will discuss an alternative detection scheme, which enables to detect such phases with the available resources.

2 Bosonic models

Describing large-scale phenomena is a challenging task. In many-body physics, the Hilbert space grows exponentially with the number of particles, making it impractical to solve the Schrödinger equation. Then, to better understand macroscopic phenomena, simplified microscopic models are proposed with the goal of capturing this large-scale behavior.

One of these examples are Hubbard models, where space is discretized as an effective lattice, and interactions are defined by two types of terms. The first is the kinetic term, captured by the tunneling term $\hat{a}^\dagger \hat{a}$ between lattice positions. The second term involves the interactions between particles, which can be either local (on-site interactions, i.e., interactions when particles occupy the same lattice sites) or non-local.

2.1 Local interactions

Historically, the approach to understanding macroscopic phenomena began with one of the simplest models, where only tunneling and local interactions are considered. Although not the most exotic system, it was sufficient to demonstrate that this methodology is practical.

2.1.1 Bose-Hubbard model

The Bose-Hubbard (BH) model [GK63] aimed to explain superconductivity, where moving electrons are modelled as bosons that propagate along discretized space. It takes the kinetic and local interactions into account, described by the Hamiltonian:

$$H = -J \sum_i \hat{a}_i^\dagger \hat{a}_{i+1} + \frac{1}{2} U \sum_i \hat{n}_i \left(\hat{n}_i - 1\right),$$

where $J > 0$ is the hopping constant, $U > 0$ is the interaction constant, $\hat{a}_i, \hat{a}_i^\dagger$ are the annihilation and creation operators acting on site i, and $\hat{n}_i = \hat{a}_i^\dagger \hat{a}_i$ is the site density. The hopping constant J resembles the tunneling between two different sites, while U comes from the collision forces between atoms in the same lattice site. For the analysis of the system, the number of particles will be the same as the lattice sites.

The hopping term favors the tunneling of the particle, while the interaction term increases the energy of the system when two particles are at the same lattice position.

Here, a competition between the two terms is observed: one favors delocalization, while the other favors localization. Depending on the magnitudes of t and U, one term will dominate over the other, resulting in two different ground states for each case. A phase transition will then appear between them.

When $J \gg U$, the hopping term dominates, and the particles will be delocalized with long range phase coherence:

$$|\Psi_{\mathrm{SF}}\rangle_{U=0} \propto \left(\sum_{i=1}^{M} \hat{a}_i^\dagger \right)^N |0\rangle, \tag{1}$$

which is called a superfluid (SF) phase.

For the case where $U \gg J$, the interaction term dominates and the particles will be localized:

$$|\Psi_{\mathrm{MI}}\rangle_{J=0} \propto \prod_{i=1}^{M} \left(\hat{a}_i^\dagger \right)^n |0\rangle, \tag{2}$$

which is a Mott insulator phase, where the movement of bosons is frozen. Here, each atoms will only occupy a specific site.

This model, thus, has two different phases. In the presented experimental setups, those are easily detected based on time-of-flight measurements [GME+02]. After the free expansion, the spatial densities are indeed the momentum densities of the original state $\langle \hat{n}_\tau(x) \rangle_\tau \approx m/(h\tau) \left\langle \hat{n}_{q(x)} \right\rangle_0$ [GJL+24]. As usual, the creation (annihilation) operators in momentum space are related to real space according to:

$$\hat{a}_{\mathbf{k}}^\dagger = \sum_{\mathbf{x}_j} e^{i\mathbf{k}\cdot\mathbf{x}_j} \hat{a}_j; \quad \hat{a}_{\mathbf{k}} = \sum_{\mathbf{x}_j} e^{-i\mathbf{k}\cdot\mathbf{x}_j} \hat{a}_j$$

The SF phase (1) is characterized by a null momentum $\mathbf{k} = 0$, while the Mott insulator, has a flat momentum distribution.

The implementation of such model in an atomic system was proposed by Cirac et al. in 1998 [CLMZ98], and experimentally proven 4 years later by Greiner et al. [GME+02]. As expected from the theoretical derivations, the SF phase was detected by a narrow momentum distribution, and the MI by a high uncertainty in the momentum measurements. From this successful realization, this approach has evolved and allowed to study the thermalization of quantum systems and transport properties.

In the meanwhile, new numerical methods have been developed to the study of such systems. Far from the limiting cases, the previous approximations no longer apply, and alternative approach are needed for their analysis. In this context, tensor networks (TN) arise, a method that exploits the entanglement structure of the state to efficiently represent them.

2.2 Frustated geometry

From the successful implementation by Greiner, experimental developments have allowed to add new interactions to the system, resulting into a richer phase diagram. Similar to the competition between t and U, the additional terms require strong numerical methods. Even if extended interactions increase the entanglement of the ground state, tensor networks are still a good choice for their study.

2.2.1 Tensor Networks

Basics of Tensor Networks

One of the biggest issues with many-body quantum systems is the size of the Hilbert space [Orú14]. For example, in a spin-1/2 system, the dimension of the space grows as 2^N, where N is the number of particles. Thus, representing such a state would require 2^N coefficients, which is not practical. As an example, writing the state of 300 spins, would require $2^{300} \approx 10^{80}$ coefficients, which is more than the number of particles in the observable universe.

The reasons is that when two particles are put in the same system, the new full Hilbert space is the tensor product between their respective spaces. This combined space is much larger than the product of spaces, as the new state can be in any superposition of the new elements of the space. Indeed, this motivates the definition of entanglement: a state is entangled if it is not a product state. Mathematically, entanglement is often measured by the von Neumann entropy. When a system is divided in two parts, this value is null if the state is a product state, and a non zero when entangled.

Despite the enormous size of the Hilbert space, it has been observed that the ground-state of local Hamiltonians actually live in a smaller region where entanglement entropy scales with the area rather than the volume of the system. This is known as the area law [Sre93].

However, the common representation of the state in the local basis does not give any intuition about its entanglement. Using a formalism where the entropy of the state is clearly presented would then be convenient, as the region with low entanglement could be only described, saving resources.

Generally, this approach is practical for low-dimensional systems. As, for instance, in a 1D Hamiltonian, the ground state's entropy remains constant, whereas in a 2D Hamiltonian, it scales with the system's length. Higher-dimensional systems, though, are less suitable for this formalism.

In this work we will only focus on 1D Hamiltonians, which are well described with the MPS representation [VC06]. Higher dimensional TN calculations are the focus of ongoing research, and will not be the focus of this work.

MPS representation

In this section we present an intuitive description of the TN method used find an economical representation of the ground-state of the Hamiltonian. A more mathematical derivation of the method is presented in Appendix A.1

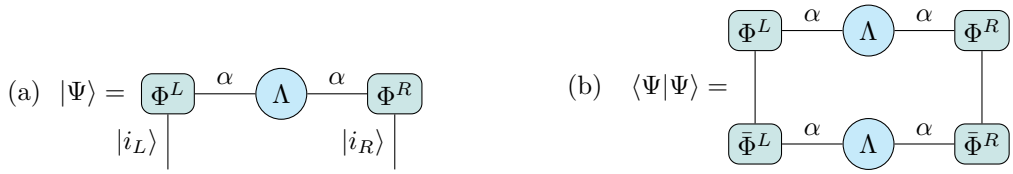

Figure 1: (a) Diagrammatic representation of Schmidt decomposition. (b) Diagrammatic representation of inner product

To exploit the low entanglement of these states, it is essential to understand the relationship between entanglement and the representation of a state. For a given partition in a left and right regions, L/R, the measure of entanglement is given by the von Neumann entropy:

$$S = -\operatorname{Tr}\left(\rho^{L/R}\log\rho^{L/R}\right) = -\sum_{\alpha}\Lambda_{\alpha}^2\log\Lambda_{\alpha}^2$$

where $\rho^{L/R}$ is the partial density matrix. In the last step the Schmidt decomposition has been used:

$$|\Psi\rangle = \sum_{\alpha=1}^{D}\Lambda_{\alpha}\left|\Phi_{\alpha}^L\right\rangle\otimes\left|\Phi_{\alpha}^R\right\rangle = \sum_{\alpha=1}^{D}\sum_{i_L,i_R}\Lambda_{\alpha}\Phi_{\alpha}^{i_L}\Phi_{\alpha}^{i_R}|i_L\rangle\otimes|i_R\rangle \to \Lambda^{\alpha}\Phi_{\alpha}^{i_L}\Phi_{\alpha}^{i_R}. \tag{3}$$

Here, the set of left $|\Phi_{\alpha}^L\rangle$ and right $|\Phi_{\alpha}^R\rangle$ vectors form an orthonormal basis for each section of the partition. In the last equality these vectors have been represented in the computational basis, being $\Phi_{\alpha}^{i_{L/R}}$ their coefficients. Λ^{α} is understood as a diagonal matrix, so only one index is shown, the other being hidden.

Due to the normalization conditions, note that $\sum_{\alpha}\Lambda_{\alpha}^2 = 1$. This implies that high entanglement is characterized by a very uniform distribution of values $\Lambda_1 \approx \Lambda_2 \approx .... \approx \Lambda_N$, while low entanglement is characterized by large differences $\Lambda_1 \gg \Lambda_2 \gg ... \gg \Lambda_N$. In the specific case of 1D gapped Hamiltonians, this decay is usually exponential. This is key for the efficient representation of states, as the state can be approximated by:

$$\left\||\Psi\rangle - \sum_{\alpha=1}^{\chi}\Lambda_{\alpha}\left|\Phi_{\alpha}^L\right\rangle\otimes\left|\Phi_{\alpha}^R\right\rangle\right\| < \epsilon$$

where $\chi < D$, so the smallest values of Λ_{α} have been removed.

The expansion in (3) is easily understood, but for more complex representations, the introduction of Penrose notation [P+71] is essential. In this notation, circles and squares represent tensors, and the legs represent indices. The connected legs indicate the contraction of indices, i.e., summation over repeated indices. The free legs, on the other hand, represent elements in the vector or dual spaces.

As a practical introduction to Penrose notation, we refer to Figure 1 (a) and equation (3). In the Schmidt decomposition of $|\psi\rangle$, an additional index α is created. To recover the original state, a summation over α needs to be performed. This is represented by the connected lines between the Λ and $\Phi^{L/R}$ tensors.

The free legs arising from $\Phi^{L/R}$ represent elements of the vector space. For each possible value of $|i_{L/R}\rangle$, the tensor $\Phi^{i_{L/R}}$ will return the corresponding coefficient. An inner product would be illustrated by repeating the same tensor structure but with the free $|i_{L/R}\rangle$ legs contracted with themselves, as in Figure 1 (b).

This dimensionality reduction can be extended to any partition of the system. For the case of 1D Hamiltonians, partitions can be performed at any site of the chain. The diagram

representation is given in Figure 2, while analytic expressions are provided in Appendix A.1. Here, the α_i represent the virtual bonds created in the decomposition, while $i_1, ..., i_N$ represent the physical degrees of freedom. In the case of a bosonic system, for example, those can represent the occupation of the lattice site. As before, $\Lambda^{[N]}$ are the Schmidt coefficients for a given partition $N-1/N$.

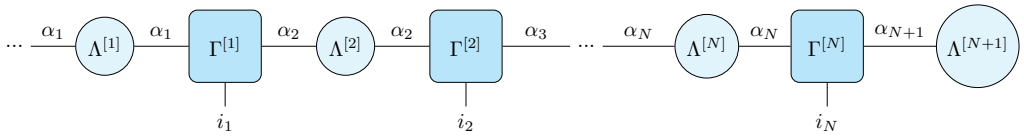

Figure 2: MPS representation of a state

This representation is dense, meaning that it can represent any state perfectly. However, it requires more coefficients than the standard representation. It only becomes useful when the values of Λ are truncated. In those cases, it saves a significant amount of memory.

Even if this representation is convenient, it is sometimes useful to gather the Λ and Γ tensors into a larger tensor by contracting their indices, as shown in Figure 3. Due to the construction of the MPS A.1, the new $A^{[i]}$ and $B^{[i]}$ tensors are isometries, so their contractions with their conjugates yield identities. This actually recovers the normalization condition, as the inner product of a state with itself is always one.

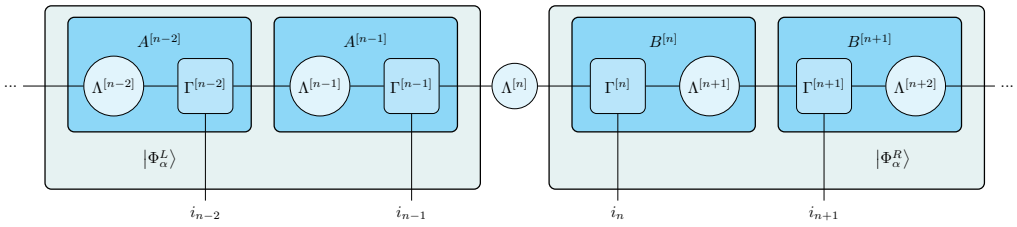

Figure 3: Canonical form of an MPS

MPO representation

In the MPS representation, only vectors in the vector space have been used. However, linear operators are composed of a vector and a dual vector.

In Penrose notation, this is represented by additional legs coming out from the tensors. In Figure 4, $O^{[i]}$ represents the local operator acting on particle i, with the indices going upwards and downwards representing the vectors and dual vectors at each position, respectively. When an operator admits this decomposition, it is called a *matrix product operator* (MPO).

The expectation value of the operator would then be computed contracting the $j_1, ...j_N$ indices with $i_1, ..., i_N$. Together with the canonical representation of the MPS, local expectation values are efficiently computed. As $A^{[i]}$ and $B^{[i]}$ are isometries, all tensor contracted with their conjugates return identities (straight lines in Penrose notation). Thus, only contractions where the operator is acting are computed, as in Figure 5.

Ground-state

So far, the problem of large Hilbert spaces has been partially solved, as ground-states of the 1D Hamiltonian lie into a small region of the space, and thus, can be efficiently represented. Nevertheless, the search for such states is still challenging due to frustration effects between phases.

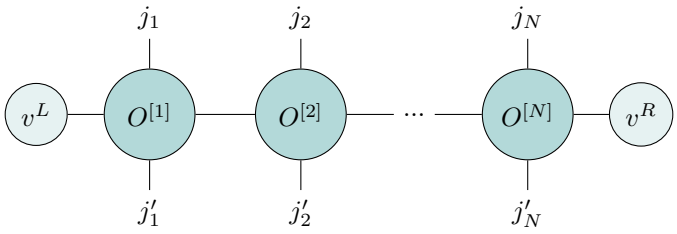

Figure 4: MPO representation of an operator.

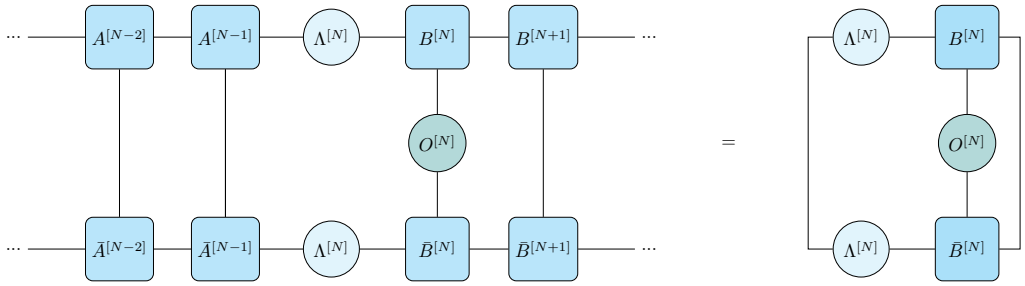

Figure 5: Simplification of expectation value computation

To find them, more properties of these systems have to be exploited. One is that a ground state with the same symmetries as the Hamiltonian can be found. Therefore, provided translational symmetry, if only two-body, nearest neighbour interactions contribute to the Hamiltonian, the system's energy is determined by the reduced density operator of these two sites [VC06].

On the other hand, the variational principle, which states that for a ground state $|\psi\rangle$:

$$\frac{\langle\Psi|H|\Psi\rangle}{\langle\Psi|\Psi\rangle} \geq E_0$$

is satisfied, suggests that the total energy can be decreased by minimizing the energy of two neighbouring particles, taking the rest as fixed. Repeating this process with the rest of the particles would lead to the ground state.

Putting these concepts together, White proposed the Density Matrix Renormalization Group (DMRG) algorithm to find the lowest energy state [Whi92].

DMRG

The first assumption made for this algorithm is that the Hamiltonian can be expressed as an MPO. The initial state will be represented by a random MPS (or a motivated choice for faster convergence), which will be variationally optimized to reduce the energy contribution from two neighboring sites. Repeating this process throughout the MPS will converge to the ground state [HP18].

First of all, the MPS is expressed in mixed canonical form (Figure 3). The two neighbouring sites to be optimized are contracted with the Schmidt values as shown in Figure 6 (a), resulting in the tensor in Figure 6 (b). At this point α_n and α_{n+2} are the virtual indices created in the Schmidt decomposition and are connected to other A or B tensors. The j_n and j_{n+1} are physical legs connected to the MPO, i.e. the Hamiltonian.

At this point, all the Hamiltonian except these four legs are contracted. For optimization purposes, $H_L^{[N]}$, $H_R^{[N+1]}$ and the local operators $O^{[N]}, O^{[N+1]}$ are left uncontracted as shown in Figure 6 (c), but this is just by choice.

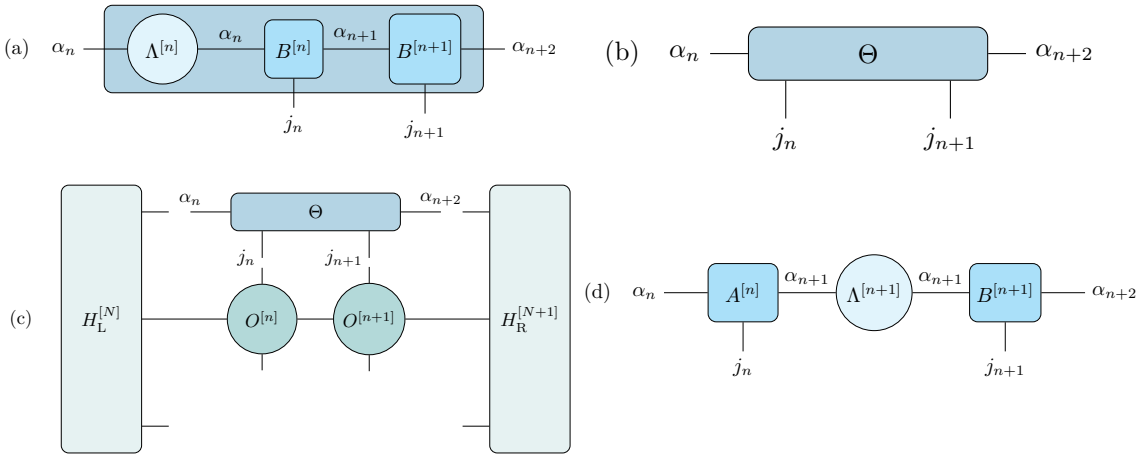

Figure 6: (a) Tensor gathering two lattice positions. (b) Tensor to optimize. (c) Effective Hamiltonian and matrix multiplication. (d) SVD decomposition after minimization

Notice that vectorizing the state Θ and the MPO results in a usual matrix multiplication with a vector (the state with four legs is contracted with the Hamiltonian, but another state with four legs is created) with dimensionality $\chi^2 d^2$, where χ and d are the dimensions of α_i and j_i respectively. This is much lower than the original Hamiltonian, so the optimization can be effectively done.

The minimization of the energy is achieved by taking the vector $\tilde{\Theta}$ with the lowest eigenvalue. For the optimization, as the full diagonalization might be expensive for large $\chi_{\max}$, variational algorithms such as Lanczos [Lan50] might be useful.

Afterwards, the Singular Value Decomposition (SVD) is computed to recover the structure of the canonical MPS, Figure 6 (d). Now, the values of the Schmidt decomposition are in $\Lambda^{[N+1]}$, already moved one position to the right to apply the next iteration. Finally, the smallest values are truncated to keep the maximum bond dimensions fixed to χ, only keeping the indices associated to the largest eigenvalues. Analytical details of the algorithm are provided in the Appendix A.4.

These steps are repeated with the next pair of tensors, until the ground state is reached. Some criteria are needed to decide when the state is converged, usually based on small variation of the energy is used.

Time evolution

DMRG gives access to the ground state of the Hamiltonian, but time-evolution of states keeps unsolved, which can be crucial for some scenarios. According to quantum mechanics, this is given by:

$$|\psi(t)\rangle = U(t)|\psi(0)\rangle.$$

where $U(t) = \exp\left(-it\hat{H}\right)$. A naive approach would be to take the exponential of the Hamiltonian's matrix form, and then apply it to the state. However, this encounters the same problem of the large Hilbert space, which suggest that an alternative method is necessary. In the majority of cases, Time Evolution Block Decimation (TEBD) is used (a detailed description is given in Appendix A.3), whose key contribution is the truncation of the lowest Schmidt values after each interaction, keeping the MPS representation effective.

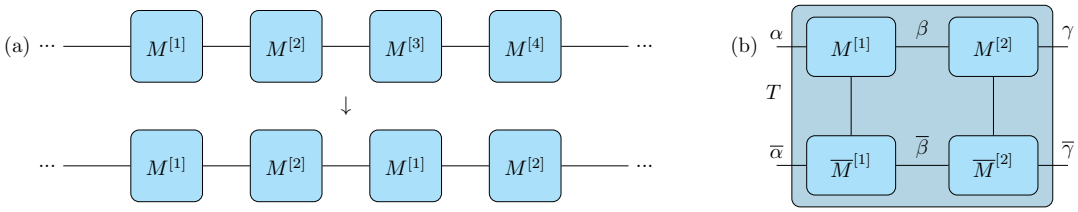

Figure 7: (a) Simplification of the MPS after applying the translational symmetry (b) Transfer matrix diagram

Infinite case

Finite size simulations provide valuable insights into the behavior of specific systems. However, such simulations can be affected by finite size effects, potentially altering the system's properties. Quantum phase transitions, and particularly the non-analytical behavior of the order parameters, are observed only in the thermodynamic limit. In this section, we introduce the generalization of the MPS designed to handle infinite systems.

One approach to tackle this is by considering the symmetries of the Hamiltonian. Usually, for local interactions, the Hamiltonian has a translation symmetry. Thus, the ground state will also have this translational symmetry. This means that $A^{[n]} = A^{[n+L]}\ \forall n$ with L being the translation length Figure 7 (a). This facilitates the calculations, as only one unit cell needs to be effectively computed.

Computing expectation values of this state might look hard. For the finite case, orthonormality conditions of the Schmidt decomposition restores identities at the edges, so only the local operator have to be applied (recall Figure 5). For the infinite case, though, it is not possible to contract the edges of the MPS.

For this analysis, it is useful to define a new tensor called *transfer-matrix* (Figure 7 (b)), which is the contraction of the unit cell with its conjugate. The spectral decomposition (in Penrose notation) is shown in Figure 8.

Now, the orthonormality conditions of the Schmidt decomposition imply that the greatest eigenvalue is one, while others $\eta_2, \eta_3, ...$ are strictly smaller. This expansion is handy, as powers of the transfer matrix are computed just taking powers of the eigenvalues. At the same time, it gives a good intuition of the behaviour of correlation functions as $\langle\psi|O_n O_m|\psi\rangle$.

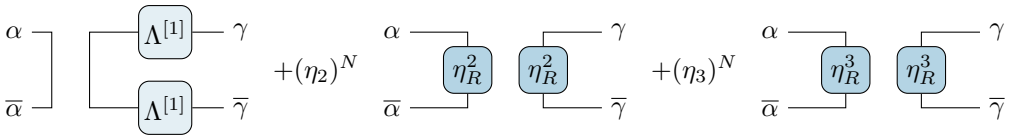

Figure 8: Eigenvector expansion of the transfer matrix

When $n \ll m$ or $n \gg m$, the reconstruction of the state is achieved introducing many transfer matrices between the corresponding O_n, O_m tensors. Knowing that the greatest eigenvalue of the transfer matrix is one, its powers will tends to $\delta_{\alpha\bar{\alpha}}\delta_{\gamma\bar{\gamma}}$, with a small correction proportional to $(\eta_2)^N$.

On the other hand, the correlation length, with captures the exponential decay of correlations with respect to the length, is closely related to η_2 A.5.

$$\langle\Psi|O_n O_m|\Psi\rangle = C \exp\left(\frac{NL}{\xi}\right) \Rightarrow \xi = -\frac{L}{\log|\eta_2|}$$

Which means that for distances greater than ξ, the operators $\langle\psi|O_n O_m|\psi\rangle$ can be (very effectively) approximated by:

$$\langle\psi|O_n O_m|\psi\rangle = \langle\psi|O_n|\psi\rangle\langle\psi|O_m|\psi\rangle \tag{4}$$

With the unit cell defined, the DMRG and TEBD algorithms can be generalized to take the thermodynamic limit into account [Sch11][Vid07]. The main difference, is that the edges have to be considered, such that when two unit cells are put next to each other, the edges still represent the bond between two lattice sites $(L, L+1) \equiv (L, 1)$.

2.2.2 Frustated Extended Bose-Hubbard

Once the appropriate numerical methods for the system are established, systems with more interactions can be analyzed.

One choice of adding a nearest neighbor interaction to the Bose-Hubbard model is proposed by the Frustated Extended bose Hubbard model (FEBH) [BCJ+23]. This system represents a geometrically frustrated many-body system, where an extended tunneling to a second-neighbor site is possible. This can occur, for example, in zig-zag atomic configurations where there is some overlap between the wavefunctions that are two-sites apart [GSV13]. It is characterized by the following Hamiltonian:

$$H_{\text{FEBH}} = -\sum_j \left[J_2\left(a_j^\dagger a_{j+2} + \text{ h.c. }\right) + J_1(-1)^j\left(a_j^\dagger a_{j+1} + \text{ h.c. }\right)\right] + \frac{U}{2}\sum_j n_j\left(n_j - 1\right).$$

As usual, J_1 is the nearest neighbour tunneling, whose alternating sign is defined by a gauge transformation, J_2 is next-nearest neighbour tunneling, U is the on-site interaction and V is the nearest neighbour interaction.

To better understand this system, first, consider the case where $J_2 \ll J_1$. In this case, the Bose-Hubbard model is almost recovered, with the only difference of the gauge $\hat{b}_j \to \exp^{i(j^2-j)\pi/2}\hat{b}_j$ in the creation and annihilation operators. Thus, a SF is recovered, but with a non zero momentum. The SF is captured by the non-zero value of the long range correlator defined as:

$$g^1(|i-j|) = \left\langle b_i^\dagger b_j \right\rangle$$

When J_2 is switched on, the behavior is similar to the J_1, but without the alternating sign. Thus, a SF is still present, but with a null momentum. This frustation will be captured by a SF which phase is neither of both, called chiral SF. Such phases are characterized by a complex phase between lattice points, captured by the local order parameter (LOP) $\langle\kappa_i\rangle$ [GSV13] , with $\kappa_j = \frac{i}{2}\left(b_j^\dagger b_{j+1} - \text{h.c.}\right)$.

Nevertheless, the Hamiltonian does not break the symmetry, so the actual ground state will be a superposition of both symmetry sectors. As a consequence, this chirality will only be observe when the computing the correlator defined as:

$$\kappa^2(|i-j|) = \langle\kappa_i\kappa_j\rangle\,.$$

This creates a competition between the SF and chiral SF, such that a new phase, the bond-order wave (BOW) appears between them. It is characterized by localized particles which are in a superposition between two neighboring lattice site. The LOP capturing this phase is:

$$\Delta B = \frac{1}{L}\sum_j \langle B_j + B_{j+1}\rangle\,,$$

where $B_j = \left(b_j^\dagger b_{j+1} + b_{j+1}^\dagger b_j\right)$. The three phases are shows in Figure 9 (a), (b) and (c). As expected, for low J_2 there is a superfluid phase, and for large J_2 the chiral superfluid arises. Due to the frustation effects, the BOW appears between both phases.

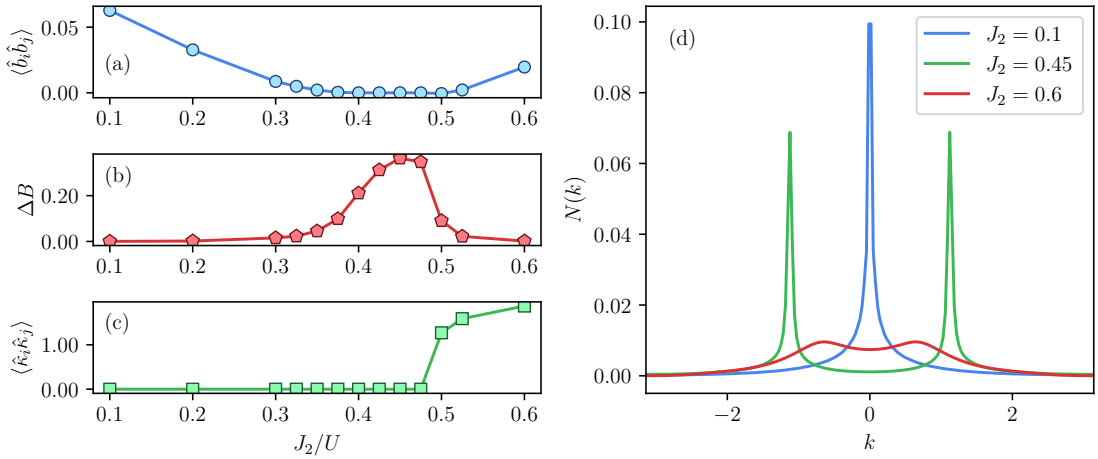

Figure 9: Parameters for the detection of the (a) SF, (b) BOW and (c) CSF phases. (d) Momentum distribution of the ground states for different values of J_2 *Parameters*: $U = 6J_1, \chi_{\max} = 200$

Experimental detection

As mentioned, the efforts made to improve quantum simulators have grown. Those, however, present a big problem when adding new type of interactions. In some cases, they imply putting particles very close to each other.

While using a microscope is the best way to detect positions, it is highly limited by the diffraction limit. As the resolution becomes insufficient, the positions can not be resolved. Thus, adding new interactions reduces the spatial resolution of particles.

The solution, first proposed in [GME+02], is to let the particles expand freely, such that their relative distances become larger, allowing for a spatial resolution. The drawback is that the momentum space is accessed rather than the usual position space.

For the Bose-Hubbard model, this is not a problem at all. For the SF phase, all the particles are in a superposition of different lattice sites, which translate into a big peak in the momentum space, meaning that a clear signal will be observed after the free expansion. For the Mott Insulator, though, particles are highly localized. Moving into momentum space, this translates into a flat distribution of momenta, without any clear peak.

The FEBH shows a slightly more challenging spectrum of phases: two superfluids and a localized phase. As stated, the SFs show a peak in the momentum distribution, but the BOW does not due to the localization of the atoms, as shown in Figure 9 (d). In this particular system, the spectrum is enough to differentiate between the three phases. However, there might be some issues if more localized phases were present, as the momentum distribution would not allow one to identify such phases. Thus, alternatives strategies are needed to successfully detect them. To develop them, systems with more localized phases are needed, which usually arise when the non-local interactions are considered.

3 Fermionic systems

Bosons have historically been a good starting point in condensed matter physics due to their relatively simple behavior and well-understood phenomena. Nevertheless, fermions also exhibit some of the exotic phases of bosonic systems, attracting significant attention. For some particular systems, fermions even show richer phase diagrams.

3.1 Non-local interactions

With the goal of developing the protocol to classify phases, a more complex system is presented. Indeed, interesting phenomena and phases arise when extended range interaction are added [MW66].

3.1.1 Extended Fermi Hubbard

A good example of a system with several localized phases is the Extended Fermi Hubbard (EFH) model. This model of spinful fermions is described by following Hamiltonian:

$$\hat{H} = -J\sum_{i,\sigma}\left(\hat{c}^{\dagger}_{i\sigma}\hat{c}_{i+1\sigma} + \text{ H.c. }\right) + V\sum_{i}\hat{n}_i\hat{n}_{i+1} + U\sum_{i}\hat{n}_{i\uparrow}\hat{n}_{i\downarrow} + J_z\sum_{i}\hat{S}^z_i\hat{S}^z_{i+1}$$

where $\hat{c}^{(\dagger)}_{i,\sigma}$ is the annihilation (creation) operator of a fermion in position i and spin σ, which can be $\uparrow$ or $\downarrow$, and $\hat{S}^z_i = (\hat{n}_{i\uparrow} - \hat{n}_{i\downarrow})/2 = \left(\hat{c}^{\dagger}_{i\uparrow}\hat{c}_{i\uparrow} - \hat{c}^{\dagger}_{i\downarrow}\hat{c}_{i\downarrow}\right)/2$ is the spin operator. Here, the fermionic behavior of the particles, as well as their spin, needs to be taken into account. A pictorial representation of the terms is shown in Figure 10

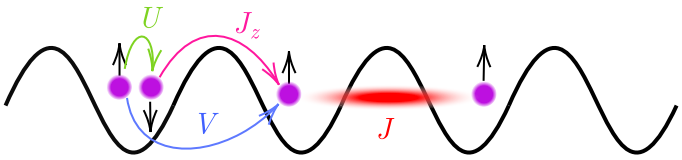

Figure 10: Schematic of the three main terms of the Hamiltonian: U is the on-site interaction, V the nearest neighbor interaction, J is the tunneling and J_z the spin interaction

As it happened with the bosonic systems, the first term corresponds to the hopping of the particles through the lattice. The second term is the nearest neighbor interaction, which gives an energy penalty if two neighboring sites are occupied at the same time. The on-site interaction term, though, is slightly different from the previous case. Here, due to the Pauli exclusion principle, only two particles of different spins are allowed at each position. Finally, the spin interaction between particles is also included.

For the analysis of the phases, $U = 4$, $J_z = 0.5$ and $J = 1$ will be used. The same number of fermions as the lattice positions $N = L$ will be considered, half of them for each spin component. The U and J are fixed such that the spatial localization of different spin fermions is energetically favored.

The parameter of interest in this model is V, the nearest neighbor interaction. For small values V, the dominant term is the interaction U between particles, so the uniform distribution of atoms minimizes the energy. Additionally, the spin interaction will force the anti-alignment of spins. This will create an *antiferromagnetic* (AF) phase, where symmetry breaking lead to two possible ground-states: $|\uparrow\downarrow\uparrow\downarrow ...\rangle$ and $|\downarrow\uparrow\downarrow\uparrow ...\rangle$. This is captured by the LOP:

$$S_z = \frac{1}{L}\sum_{i}(-1)^i\left\langle\hat{S}^z_i\right\rangle,$$

which gives a larger value if the spins of neighbouring sites are antialigned.

One can observe that this is an example of symmetry breaking, where the translational invariance of the Hamiltonian has been spontaneously broken into two possible symmetry sectors. Such phases are called spontanously symmetry broken (SSB) phases, and the symmetry breaking, indeed, provides an easy path for their detection: checking if the

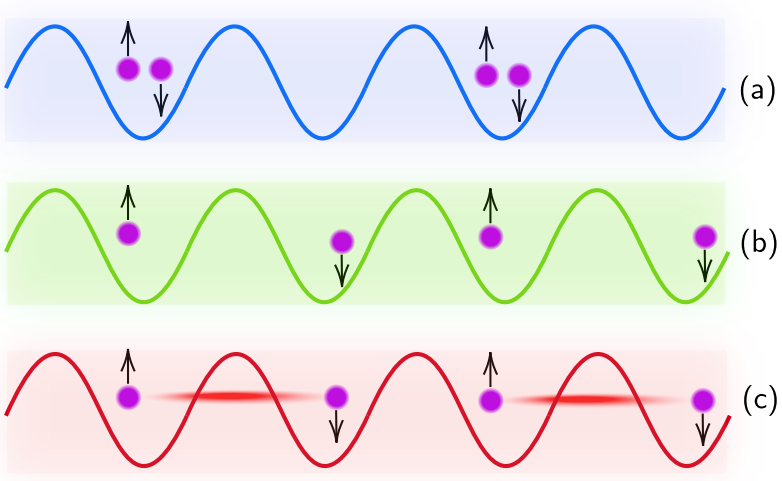

Figure 11: Phases of the EFH model. (a) is the CDW, (b) is the AF and (c) is the BOW

ground state has broken a specific symmetry of the Hamiltonian, which is indeed, the LOP.

For large V, though, the nearest neighbor interaction dominates over the on-site one, and occupying neighboring sites is energetically more expensive. This will create a phase called *charge density wave* (CDW), characterized by the alternating density of fermions in the lattice. The symmetry breaking is characterized by the occupation between the even or odd positions of the lattice. This is captured by the LOP:

$$S_c = \frac{1}{L}\sum(-1)^i \left\langle \hat{n}_{i\uparrow} + \hat{n}_{i\downarrow} \right\rangle /2,$$

which gives the largest value if the density has a periodicity of two.

As in the previous case, the competition of this two phases creates an additional phase between them: the BOW. Here, in the same way as with the FEBH, particles will be in a superposition of two neighboring lattice sites. Additionally, this bond occupation will vary every two positions. The only difference from the FEBH, is the chosen gauge. Here, as J is constant for all the positions, so the LOP is:

$$B = \frac{2}{L}\sum_{i\sigma}(-1)^i b_{i\sigma}$$

with $b_{i\sigma} = \hat{b}_i^\dagger \hat{b}_{i+1} +$ h.c. The phase diagram can be observed in Figure 12, while the pictorial representations of the phases in Figure 11. The experimental detection of such phases, though, is not properly achieved with the momentum distribution, as all of them would give a gaussian distribution, due to the localization of the states. For a good detection of the states, correlations between momenta should be accessed.

3.1.2 Noise Correlation Measurements

A usual definition of such correlators are called noise correlation measurements (NCM) [ADL04] :

$$N(q) = 1 - \frac{\langle n_k n_{k+q} \rangle}{\langle n_k \rangle \langle n_{k+q} \rangle}$$

where n_k defines the density operator of states with momentum k. As these are measured through a time-of-flight measurement, the spatial densities obtained after some ballistic

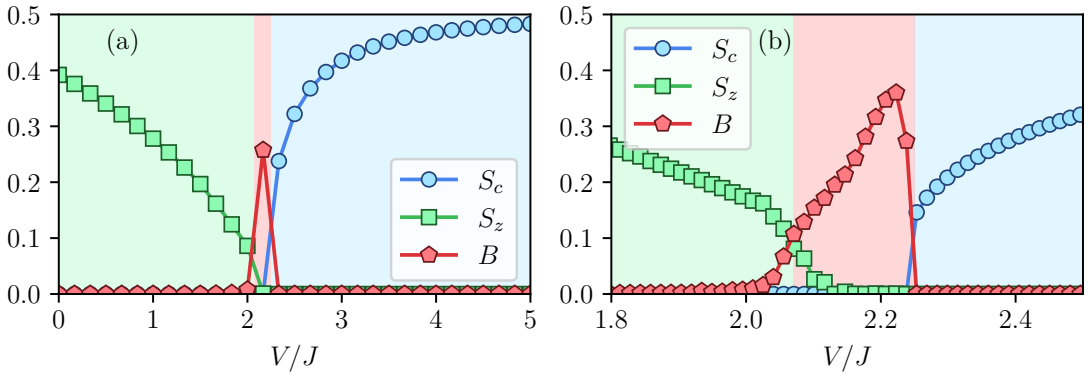

Figure 12: LOP parameters of the three phases of the Extended Fermi Hubbard model. *Parameters:* $J = 1.0, U = 4.0, J_z = 0.5$

expansion are indeed the momentum densities of the original state [GJL+24] $\langle \hat{n}_\tau(x) \rangle_\tau \approx m/(h\tau) \left\langle \hat{n}_{q(x)} \right\rangle_0$. Then, the noise correlator transforms into:

$$N(d) = 1 - \frac{\int dx \langle \hat{n}(x + d/2) \cdot \hat{n}(x - d/2) \rangle_\tau}{\int dx \langle \hat{n}(x + d/2) \rangle_\tau \langle \hat{n}(x - d/2) \rangle_\tau}.$$

This density correlations, expressed in terms of the $\hat{c}^{(\dagger)}_{i,\sigma}$ annihilation (creation) operator of a fermion in positioni and spin σ, result into an already simplified noise correlator:

$$N(d) = 1 - \frac{\sum_{rsr'} \left\langle \hat{c}^\dagger_{r,\sigma} \hat{c}_{s,\sigma} \hat{c}^\dagger_{r',\sigma'} \hat{c}_{r'+r-s,\sigma'} \right\rangle e^{iQ(d)[(r-s)]}}{\sum_{rsr'} \left\langle \hat{c}^\dagger_{r,\sigma} \hat{c}_{s,\sigma} \right\rangle \left\langle \hat{c}^\dagger_{r',\sigma'} \hat{c}_{r'+r-s,\sigma'} \right\rangle e^{iQ(d)[(r-s)]}}, \tag{5}$$

This would allow one to start the analysis of such phases, but the computational cost is challenging. Even if it has been reduced from $\mathcal{O}(N^4)$ expectation values to $\mathcal{O}(N^3)$, the cost grows too fast for large systems. As the main objective of this thesis is to make our calculations with systems as large as possible, further improvements are needed.

Optimization

There are several properties that can be exploited to reduce the computational cost when using TNs. The first is the translational symmetry of the iMPS, that, even in these SSB phases, repeat every two sites. Therefore, for this system, the iMPS is reconstructed from a single unit cell with length two, meaning that all expectation values translated by two lattice sites are the same:

$$\left\langle c^\dagger_{r,\sigma} c_{s,\sigma} c^\dagger_{r',\sigma} c_{s',\sigma} \right\rangle = \left\langle c^\dagger_{r+2i,\sigma} c_{s+2i,\sigma} c^\dagger_{r'+2i,\sigma} c_{s'+2i,\sigma} \right\rangle \quad \forall i \in \mathbb{N}.$$

Applying this property to the correlation function, the numerator becomes:

$$\sum_{rsr'} \left\langle \hat{c}^\dagger_{r,\sigma} \hat{c}_{s,\sigma} \hat{c}^\dagger_{r',\sigma'} \hat{c}_{r'+r-s,\sigma'} \right\rangle = \sum_{r,s} \left[\left\langle c^\dagger_{0,\sigma} c_{s,\sigma} c^\dagger_{r,\sigma'} c_{r-s,\sigma'} \right\rangle + \left\langle c^\dagger_{1,\sigma} c_{s,\sigma} c^\dagger_{r,\sigma'} c_{r-s,\sigma'} \right\rangle \right] N_{\text{tr}}, \tag{6}$$

where r, s go from $-N$ to N, with the condition that the expectation value lies within the limits of the reconstructed state, e.g. , if the noise correlator for $N = 8$ is being computed, the expectation value $\left\langle c^\dagger_{0,\sigma} c_{3,\sigma} c^\dagger_{7,\sigma'} c_{4,\sigma'} \right\rangle$ is allowed, but $\left\langle c^\dagger_{0,\sigma} c_{3,\sigma} c^\dagger_{-3,\sigma'} c_{-6,\sigma'} \right\rangle$ is not. N_{tr} is the number of times that this expectation value is repeated within the chain.

Regarding the number of expectation values, this already improves the initial computational cost from $\mathcal{O}(N^3)$ to $\mathcal{O}(N^2)$. Nevertheless, there is one additional problem to this computations. When the expectation value for a larger system is computed, the number of tensor contractions also grows, implying an additional cost that will rapidly becomes inconvenient for large systems.

This problem can slightly be tackled considering the structure of the iMPS and the shape of equation (6). If s is fixed, the changing value of r only affects the last two operators. As the iMPS is divided into tensors, this allows to re-use computations performed in previous cases.

Take, for example, the expectation value of $\left\langle c^\dagger_{0,\sigma} c_{1,\sigma} c^\dagger_{3,\sigma'} c_{2,\sigma'} \right\rangle$. Notice that the following expectation values $\left\langle c^\dagger_{0,\sigma} c_{1,\sigma} c^\dagger_{3+r,\sigma'} c_{2+r,\sigma'} \right\rangle$, with r even, are computed introducing transfer matrices between the operators. Thus, saving in memory the partial contractions of the operators with the transfer matrices, avoids repeating previously performed calculations.

Even if the implementation is not straightforward, as there are many details to take into account (Appendix B), those are very useful when computing NCM for large system. Figure 13 shows the computational time of the NCM for different number of particles N with three methods.

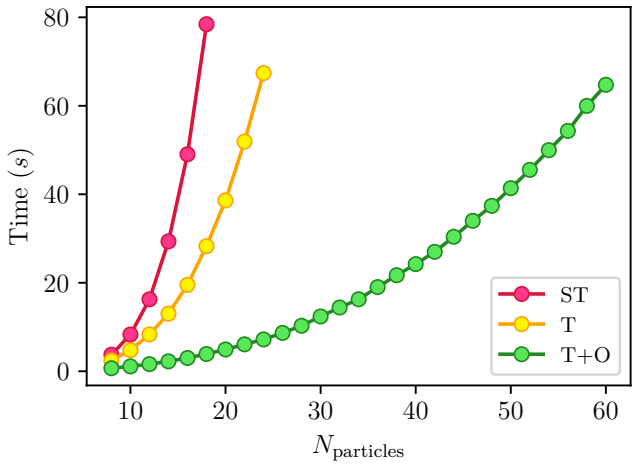

Figure 13: Computation time of the NCM vs. N for different methods. ST is using (5), T is the using translation symmetry (6), and T+O with all the optimizations from Appendix B.

Experimental detection

This NCM give additional information about the states. The momentum distribution of Figure 14 shows that atoms are highly localized, due to the gaussian-like distributions. Nevertheless, it does not give any intuition of the state. The correlation measurements, instead, show that momenta with a difference of $d = \pi$ are correlated. This means that for each spin occupation, or tunneling, there is an alternating occupation every two positions. Assuming that the correlation are short range and the states are perfectly converged, the noise correlations measurement can be simplified to [GJL+24]:

$$N(\nu\ell/2) = \frac{\sum_\sigma \left[\sum_r (-1)^{\nu r} n_{r\sigma}\right]^2 + 0.5 \sum_\sigma \left[\sum_r (-1)^{\nu r} b_{r\sigma}\right]^2}{\left(\sum_{\sigma r} n_{r\sigma}\right)^2 - 0.5 \left(\sum_{\sigma r} b_{r\sigma}\right)^2}$$

where $n_{r\sigma}$ denotes the occupation of particles in site r and $b_{r\sigma} = \left\langle \hat{c}^\dagger_{r\sigma} \hat{c}_{r+1\sigma} + \text{h.c.} \right\rangle$. This clearly shows that the three phases give a non-zero value of the NCM for $d = \pi$.

This is an important fact because the Extended Fermi Hubbard has three SSB phases which show this dimerization. Obviously, the dimerization is closely related to the broken symmetry of the state. One possible way of detecting such phases would be decreasing or increasing the energy of each symmetry sector. If the dimerization is affected due to this change, it means that this broken symmetry this symmetry was already broken. If it is unaffected, it is not.

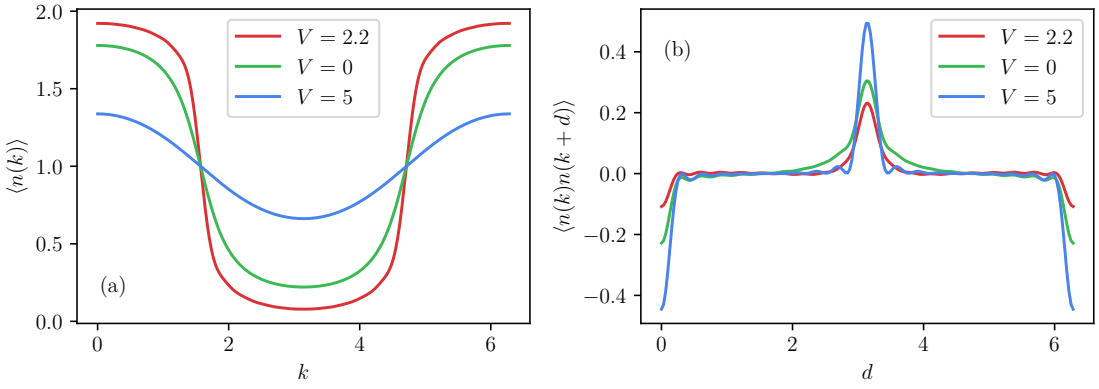

Figure 14: (a) Momentum distribution and (b) correlation function of the Extended Fermi Hubbard model. The momentum distribution shows the localization of the particles, while the correlations show the periodicity in the lattice.

This subtle idea can be exploited to identify the three phases, but more details are needed for that.

3.1.3 Lattice modulation

As stated, the NCM for the Fermi-Hubbard model shows the dimerization of the three phases, but the signal might actually correspond to any of them. The connection between NCM and the broken symmetry of each phase, though, could help classifying them.

As explained in the theory part, these phases are SSB phases. Thus, there is a LOP associated with each of them. Even if these observables are not accessible experimentally, their corresponding operators can be added to the Hamiltonian.

The point comes from the fact that for each phase, there is one symmetry which is broken (the one captured by the LOP), that is not broken by the other two phases. If this symmetry is artificially broken in the Hamiltonian, the states will change according to their phase. The objective is to understand how it will be affected if the evolution is adiabatically carried out.

If the added term corresponds to the broken symmetry and it reduces the energy of the present symmetry sector, the state will remain unchanged along this adiabatic evolution. However, if the opposite symmetry sector is favoured, the state cannot reach adiabatically the new ground state of the hamiltonian, as the gap closes along that path.This will resulting into a state with a completely different value of the NCM, as the dimerization will be lost.

If the phase does not correspond to the artificially broken symmetry, there is no preferred symmetry sector. This means that the final state will be the same for both paths and their final NCM will be equal.

At this point, this gives enough information to know which phase the system is at. After carrying out the time evolution for the different sectors of the LOP, if the NCM show

a different value, the the phase will be the one corresponding to the LOP.

To illustrate this methodology, consider the case of the AF. The LOP is:

$$S_z = \frac{1}{L}\sum_i (-1)^i \left\langle \hat{S}_i^z \right\rangle = \frac{1}{2L}\sum_i (-1)^i \left(\hat{n}_{i\uparrow} - \hat{n}_{i\downarrow}\right),$$

This means that spins tend to be anti-aligned. The broken symmetry is the spin direction in a fixed site, for example, the first spin being is up or down. This symmetry breaking term can be added to the Hamiltonian as:

$$\hat{H}_{\mathrm{AF}}(t) = -\Delta_{\mathrm{AF}}(t) \sum_{i\in^{\mathrm{even}}_{\mathrm{odd}}} \left(\hat{n}_{i\uparrow} - \hat{n}_{i\downarrow}\right),$$

where $\Delta_{\mathrm{AF}} = -10(t/T)^2$, with $T = 50$, and $t \in [0, 7.5]$ carries out the lattice modulation. If the ground state corresponds to the one having the spin up in the first position and down in the second, the addition of this term will respect the symmetry sector, and the adiabatical evolution will keep the state unchanged.

If the added term was the opposite (down in position zero and up in one), the gap would need to close before reaching the ground-state of the new hamiltonian, which cannot be adiabatically followed. At this point, the state will mix with the rest of the spectrum, directly affecting its dimerization. The NCM of both lattice modulations will consequently show a different value after each of the two possible paths. One should note that, in an experiment, the breaking of the symmetry occurs spontaneously, and one does not know which of the sectors is present. Therefore, the presence of a SSB phase will manifest as a bimodal distribution of NCMs.

Figure 15 shows that the LOP after the two possible modulations only end up with a different value if the added term corresponds to the same LOP.

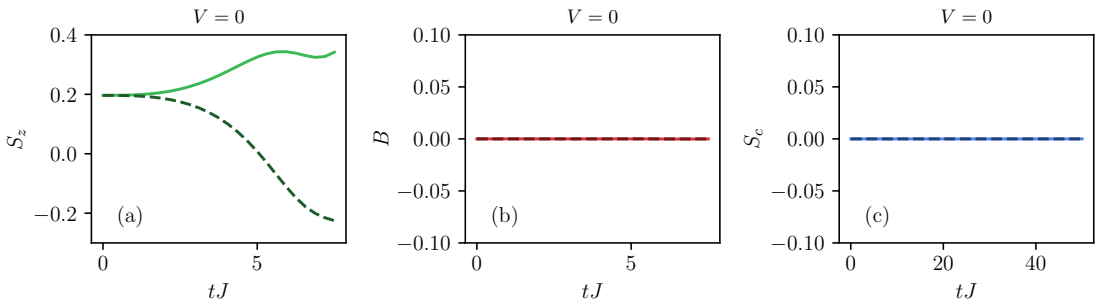

Figure 15: Evolution of the LOP for the two possible symmetry sectors associated with each LOP, (a) for the AF, (b) for the BOW and (c) for the CDW. As $V = 0$, the ground states is in the AF phase, and only the time-evolution associated with the AF separates both LOP

For the CDW, the methodology is analogous. The LOP is:

$$S_c = \frac{1}{L}\sum (-1)^i \left\langle \hat{n}_{i\uparrow} + \hat{n}_{i\downarrow} \right\rangle /2 = \frac{1}{2L}\sum_{i\sigma} (-1)^i \langle \hat{n}_{i\sigma} \rangle = \frac{1}{2L}\sum_{\sigma} \langle \hat{n}_{e,\sigma} - \hat{n}_{o,\sigma} \rangle.$$

This captures the non-uniform occupation of even and odd sites. Thus, the broken symmetry is between occupation of even and odd sites. The additional term to break the symmetry of the Hamiltonian is:

$$\hat{H}_{\mathrm{CDW}} = -\Delta_{\mathrm{CDW}}(t) \sum_{\sigma, i\in^{\mathrm{odd}}_{\mathrm{even}}} \hat{n}_{i,\sigma},$$

where $\Delta_{\mathrm{CDW}}(t) = (t/T)^2$, with $T = 50$ carries out the adiabaticall expansion.

For the BOW, the same strategy can be carried out. Starting form the LOP:

$$B = \frac{1}{L}\sum_i (-1)^i \left(\hat{b}_i \hat{b}^\dagger_{i+1} + \hat{b}^\dagger_{i+1}\hat{b}_i\right).$$

Finding the two different sectors, leads to the Hamiltonian term:

$$\hat{H}_{\mathrm{BOW}}(t) = \Delta_{\mathrm{BOW}}(t)\sum_\sigma \sum_{i\in^{\mathrm{even}}_{\mathrm{odd}}} \left[\hat{c}^\dagger_{2i,\sigma}\hat{c}_{2i+1,\sigma} + \hat{c}^\dagger_{2i+1,\sigma}\hat{c}_{2i,\sigma}\right],$$

with $\Delta_{\mathrm{BOW}} = 10(t/T)^2$, with $T = 50$ and $t \in [0, 7.5]$.

As a proof of concept, the evolution of the LOP and NCM with respect to the time has been plotted in Figure 16 for the three phases of the system. As expected, the lost dimerization directly affects the NCM, resulting into a signal when the lattice modulation is compatible with the LOP.

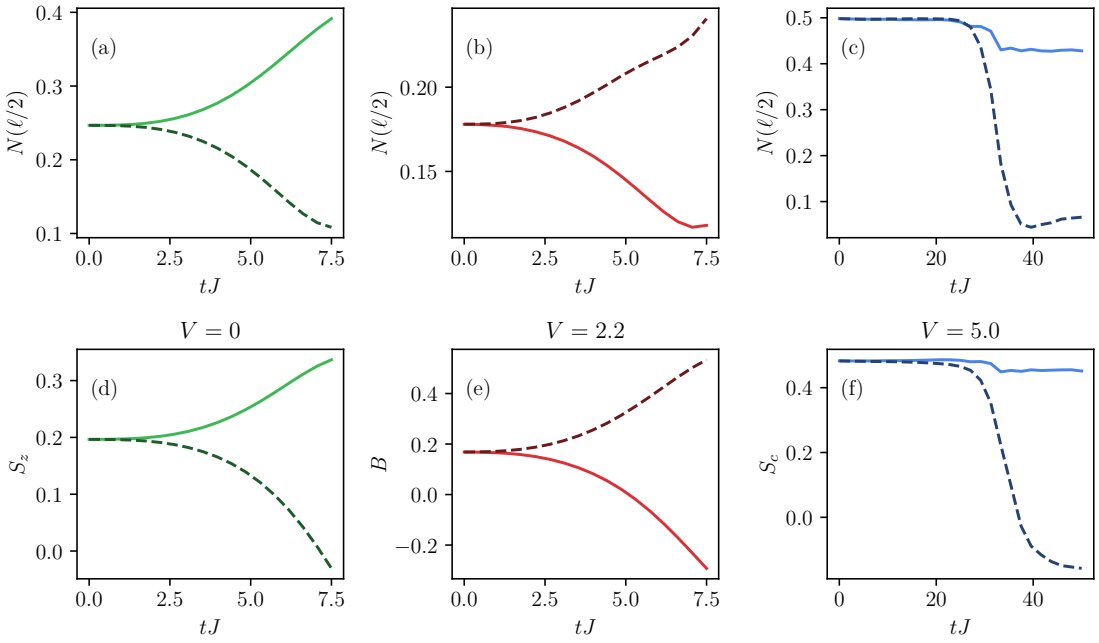

Figure 16: Evolution of the LOP (a),(b) and (c) and the NCM (d),(e) and (f) for the different sectors associated with each symmetry of the LOP. (a) and (d) correspond to the AF, (b) and (e) to the BOW, (c) and (f) to the CDW

Finally, the phase diagram can be computed. Numerical details in Appendix D. First, the ground state of the Hamiltonian is found, and then, the evolution of the two possible Hamiltonian for each phase is carried out. The different between the two paths is then plotted in Figure 17 (a).

At this point, the advantage of NCM over the momentum distribution is clear, as its signal is much more sensitive to the loss of the dimerization, as shown in Figure 18

Thermodynamic limit

Even if tensor networks and the optimization of the NCM allows one to reach $N \approx 100$ in a reasonable computation time, finite size effects are still observed in the phase diagram represented in Figure 17 while the AF and the CDW give a null value in the regimes where

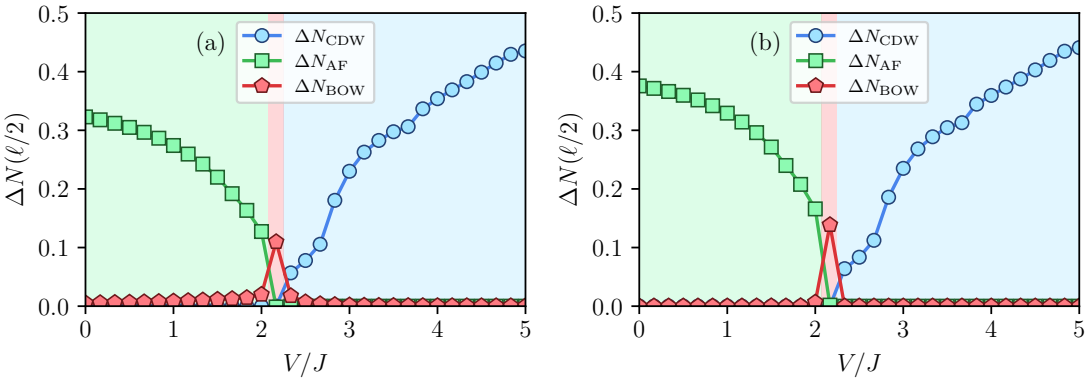

Figure 17: Difference in NCM after the two possible lattice modulation for phase. (a) is the finite case with $N = 100$, while (b) is the thermodynamic limit

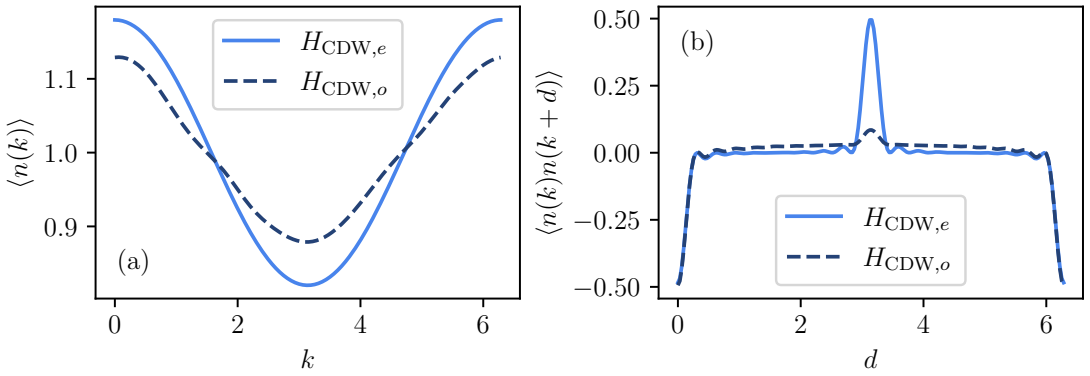

Figure 18: (a) Spectrum of momenta and (b) correlations after the evolution of the two symmetry sectors. The NCM at $d = \pi$ capture the dimerization of the particles more effectively.

the phase is not present, the BOW gives a finite value in the whole AF regime, and part of the CDW.

To solve this problem, some properties of these phases will be recovered. In SSB phases, correlations always decay for large systems. This can be clearly observed with the transfer-matrix formalism and equation (4). When two operators are far from each other, and there is no phase transition present, the main expansion of the transfer-matrix powers will be the identity, i.e. for large N, $(\eta_2)^N$ will tend to zero.

From the simplified expression of (6), it can be observed that for large N, the main contribution will correspond to $j \approx 0$ of $j \approx k$. Additionally, in most of the cases, $j \gg k$ or $j \ll k$, so the repeated projection onto the project matrix will simplify the terms to:

$$\begin{cases} \langle \hat{c}^\dagger_{0,\sigma} \hat{c}_{j,\sigma} \hat{c}^\dagger_{k,\sigma'} \hat{c}_{k-j,\sigma'} \rangle \approx \langle \hat{c}^\dagger_{0,\sigma} \hat{c}_{j\sigma} \rangle \langle \hat{c}^\dagger_{k,\sigma'} \hat{c}_{k-j,\sigma'} \rangle & \text{if } j \approx 0 \\ \langle \hat{c}^\dagger_{0,\sigma} \hat{c}_{k-j,\sigma'} \hat{c}^\dagger_{k,\sigma'} \hat{c}_{j,\sigma} \rangle \approx -\langle \hat{c}^\dagger_{0,\sigma} \hat{c}_{k-j,\sigma'} \rangle \langle \hat{c}^\dagger_{k,\sigma'} \hat{c}_{j\sigma} \rangle & \text{if } j \approx k, j \neq k \end{cases}$$

Due to the translational symmetry of the iMPS, $\langle \hat{c}^\dagger_{0,\sigma} \hat{c}_{k-j,\sigma'} \hat{c}^\dagger_{k,\sigma'} \hat{c}_{j,\sigma} \rangle$ will be the same for $k \to k+2$, resulting into the addition of the same term to the noise correlator. This gives the intuition that in the thermodynamic limit, the noise correlator converges to a given value, in particular, the one given by the contribution of distant couples of creation and annihilation operators.

Another cause of finite size effect are the boundaries. In (6), the repetitions of the same

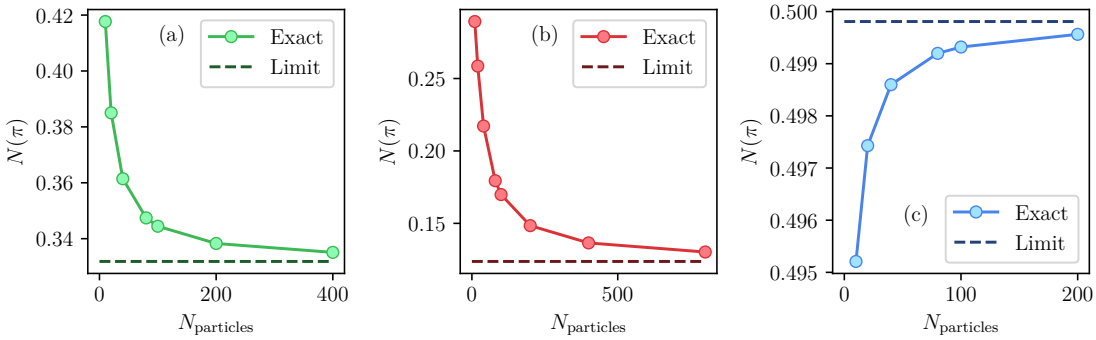

Figure 19: Exact values of the NCM compared with the proposed limit. (a) is for the AF ($V = 0$), (b) for the BOW ($V = 2.16$) and (c) for the CDW ($V = 5.0$)

observable within the chain length are considered. In the thermodynamic limit, though, one would expect all possible expectations values to be repeated the same amount of times.

Putting this concepts into practice, one can deduce that noise correlator in the thermodynamic limit will look like the one in (6), with the $N_{\text{translation}}$ the same for all cases, and using the sinplifications states above for the specific cases. The complete expression is given in Appendix C.

For the three phases, Figure 19 shows that the NCM approaches the limit for large N. This is important, because for the AF and the BOW, the exact value only approaches the proposed limit for large N, meaning that finite size effects are present even in very large systems. Using this limit, finite size effects from Figure in 17 (a) are corrected in 17 (b).

4 Conclusions

This project has proposed a new method to detect SSB phases in ultracold optical lattices, accompanied by a scaling analysis of the methodology. This approach involves understanding optical lattices and several detection techniques. To develop them, two systems have been presented and analyzed, with the goal of motivating the introduction of new concepts such as tensor networks and noise correlations measurements.

After establishing the theoretical foundation, the final methodology has been presented, highlighting the challenge of NCM calculations for large systems. To tackle it, new optimization methods have been presented and implemented. This optimization has enabled the study of systems with up to 100 particles, compared to the approximate 12 particles achievable with exact diagonalization.

Using the insights gained from this optimization, the NCM limit in the thermodynamic limit has been proposed and compared to large systemshowing good agreement. The resulting phase diagram suggests this strategy effectively identifies SSB phases even in the large system limit where current experiments operate.

The next step would be to proof that this can actually be implemented in an experimental setup. Once achieved, it would open a wide variety of possibilities, as the proposed approach is general to any phase where traslational invariance is broken. For example, the SSB phases of the 2D EFH system could be studied, as the experimental implemention should be straightforward from the 1D case, and the proposed alternative is completely applicable. This would indeed give access to information that cannot be reached within the actual numerical methods, which serves as a motivation for the experimental investigation of this advance in the field.

Bibliography

[ADL04] Ehud Altman, Eugene Demler, and Mikhail D. Lukin. Probing many-body states of ultracold atoms via noise correlations. *Phys. Rev. A*, 70(1):013603, July 2004.

[ANB77] J. Als-Nielsen and R. J. Birgeneau. Mean field theory, the Ginzburg criterion, and marginal dimensionality of phase transitions. *American Journal of Physics*, 45(6):554–560, June 1977.

[BCJ+23] Niccolò Baldelli, Cesar R. Cabrera, Sergi Julià-Farré, Monika Aidelsburger, and Luca Barbiero. Frustrated extended Bose-Hubbard model and deconfined quantum critical points with optical lattices at the anti-magic wavelength, September 2023.

[BM86] J. G. Bednorz and K. A. Müller. Possible highTc superconductivity in the Ba-La-Cu-O system. *Z. Physik B - Condensed Matter*, 64(2):189–193, June 1986.

[CLMZ98] J. I. Cirac, M. Lewenstein, K. Mølmer, and P. Zoller. Quantum superposition states of Bose-Einstein condensates. *Phys. Rev. A*, 57(2):1208–1218, February 1998.

[DDM+23] Nicolò Defenu, Tobias Donner, Tommaso Macrì, Guido Pagano, Stefano Ruffo, and Andrea Trombettoni. Long-range interacting quantum systems. *Rev. Mod. Phys.*, 95(3):035002, August 2023.

[dS03] Raimundo R. dos Santos. Introduction to quantum Monte Carlo simulations for fermionic systems. *Braz. J. Phys.*, 33:36–54, March 2003.

[DS13] H.T. Diep and W. Scientific. *Frustrated Spin Systems*. World Scientific, 2013.

[Fey82] Richard P. Feynman. Simulating physics with computers. *Int J Theor Phys*, 21(6):467–488, June 1982.

[GB17] Christian Gross and Immanuel Bloch. Quantum simulations with ultracold atoms in optical lattices. *Science*, 357(6355):995–1001, September 2017.

[GJL+24] Kerman Gallego-Lizarribar, Sergi Julià-Farré, Maciej Lewenstein, Christof Weitenberg, Luca Barbiero, and Javier Argüello-Luengo. Probing spontaneously symmetry-broken phases with spin-charge separation through noise correlation measurements, July 2024.

[GK63] H. A. Gersch and G. C. Knollman. Quantum Cell Model for Bosons. *Phys. Rev.*, 129(2):959–967, January 1963.

[GME+02] Markus Greiner, Olaf Mandel, Tilman Esslinger, Theodor W. Hänsch, and Immanuel Bloch. Quantum phase transition from a superfluid to a Mott insulator in a gas of ultracold atoms. *Nature*, 415(6867):39–44, January 2002.

[GSV13] S. Greschner, L. Santos, and T. Vekua. Ultracold bosons in zig-zag optical lattices. *Phys. Rev. A*, 87(3):033609, March 2013.

[HP18] Johannes Hauschild and Frank Pollmann. Efficient numerical simulations with Tensor Networks: Tensor Network Python (TeNPy). *SciPost Physics Lecture Notes*, page 005, October 2018.

[JGP+22] Sergi Julià-Farré, Daniel González-Cuadra, Alexander Patscheider, Manfred J. Mark, Francesca Ferlaino, Maciej Lewenstein, Luca Barbiero, and Alexandre Dauphin. Revealing the topological nature of the bond order wave in a strongly correlated quantum system. *Phys. Rev. Res.*, 4(3):L032005, July 2022.

[Lan50] Cornelius Lanczos. An iteration method for the solution of the eigenvalue problem of linear differential and integral operators. *J. Res. Natl. Bur. Stand. B*, 45:255–282, 1950.

[Lau83] R. B. Laughlin. Anomalous Quantum Hall Effect: An Incompressible Quantum Fluid with Fractionally Charged Excitations. *Phys. Rev. Lett.*, 50(18):1395–1398, May 1983.

[LSA+07] Maciej Lewenstein, Anna Sanpera, Veronica Ahufinger, Bogdan Damski, Aditi Sen De, and Ujjwal Sen. Ultracold atomic gases in optical lattices: Mimicking condensed matter physics and beyond. *Advances in Physics*, 56(2):243–379, March 2007.

[MW66] N. D. Mermin and H. Wagner. Absence of Ferromagnetism or Antiferromagnetism in One- or Two-Dimensional Isotropic Heisenberg Models. *Phys. Rev. Lett.*, 17(22):1133–1136, November 1966.

[Orú14] Román Orús. A practical introduction to tensor networks: Matrix product states and projected entangled pair states. *Annals of Physics*, 349:117–158, October 2014.

[P+71] Roger Penrose et al. Applications of negative dimensional tensors. *Combinatorial mathematics and its applications*, 1:221–244, 1971.

[Sch11] Ulrich Schollwöck. The density-matrix renormalization group in the age of matrix product states. *Annals of Physics*, 326(1):96–192, January 2011.

[SDS+23] Lin Su, Alexander Douglas, Michal Szurek, Robin Groth, S. Furkan Ozturk, Aaron Krahn, Anne H. Hébert, Gregory A. Phelps, Sepehr Ebadi, Susannah Dickerson, Francesca Ferlaino, Ognjen Marković, and Markus Greiner. Dipolar quantum solids emerging in a Hubbard quantum simulator. *Nature*, 622(7984):724–729, October 2023.

[Sre93] Mark Srednicki. Entropy and area. *Phys. Rev. Lett.*, 71(5):666–669, August 1993.

[Suz91] Masuo Suzuki. General theory of fractal path integrals with applications to many-body theories and statistical physics. *Journal of Mathematical Physics*, 32(2):400–407, February 1991.

[VC06] F. Verstraete and J. I. Cirac. Matrix product states represent ground states faithfully. *Phys. Rev. B*, 73(9):094423, March 2006.

[Vid07] G. Vidal. Classical Simulation of Infinite-Size Quantum Lattice Systems in One Spatial Dimension. *Phys. Rev. Lett.*, 98(7):070201, February 2007.

[Whi92] Steven R. White. Density matrix formulation for quantum renormalization groups. *Phys. Rev. Lett.*, 69(19):2863–2866, November 1992.

A Tensor Networks

A.1 MPS

To exploit the low entropy of this states, we need to make a partition of of the system in two parts. This is achieved by the Schmidt decomposition of a state:

$$|\Psi\rangle = \sum_{\alpha=1}^{D} \lambda_\alpha \left|\Phi_\alpha^L\right\rangle \otimes \left|\Phi_\alpha^R\right\rangle .$$

Where the set of left $|\Phi_\alpha^L\rangle$ and right $|\Phi_\alpha^R\rangle$ vector form an orthonormal basis of each of the parts of the partition. The reduced density matrix related to each partition is then:

$$\rho^{R/L} = \mathrm{Tr}_{L/R} \left(|\Psi\rangle \langle\Psi|\right)$$

Where $\mathrm{Tr}_{L/R}$ is the partitial trace over the left/right subspace. If the entanglement is measured by the von Neumann entropy, it can be measured using the Schmidt coefficients:

$$S = -\mathrm{Tr}\left(\rho^R \log \rho^R\right) = -\sum_\alpha \lambda_\alpha^2 \log \lambda_\alpha^2$$

This sets a clear relation between the Schmidt decomposition for a given partition and its entropy. However, to use the full potential of the area law, it is useful to represent all the possible partitions at the same time. To achieve this, note that any state can be represented in the computational basis by:

$$|\Psi\rangle = \sum_{i_1 i_2 \ldots i_N} C_{i_1 i_2 \ldots i_N} |i_1\rangle \otimes |i_2\rangle \otimes \cdots \otimes |i_N\rangle$$

Where the $i_1 ... i_N$ indices represent the physical index of the Hilbert space. Based on the Schmidt decomposition for each possible partition, and expressing the left and right vectors in the computational basis, it is recover [Orú14]:

$$C_{i_1 i_2 \ldots i_N} = \Lambda^{[1]}_{\alpha_1} \Gamma^{[1] i_1}_{\alpha_1 \alpha_2} \Lambda^{[2]}_{\alpha_2} \Gamma^{[2] i_2}_{\alpha_2 \alpha_3} \Lambda^{[3]}_{\alpha_3} \Gamma^{[3] i_3}_{\alpha_3 \alpha_4} \cdots \Lambda^{[N]}_{\alpha_N} \Gamma^{[N] i_N}_{\alpha_N \alpha_{N+1}} \Lambda^{[N+1]}_{\alpha_{N+1}}, \tag{7}$$

In this representeation, $i_1 ... i_N$ keeps being the physical index, but now there are some virtual bonds $\alpha_1 ... \alpha_N$. Due to the mess of indices, Penrose notation is used [P+71]. This representation corresponds to the networks in Figure 2

Note that some additional bonds have been created, which precisely correspond to the entanglement between the constituent parts. One property of such decomposition is that this representation is dense, meaning that any state can be represented by such decomposition. At a first glance, this might not effective, as the new bonds require a higher amount of parameters.

However, as the ground state of 1D Hamiltonian follow the area law, the entropy has to be obey the area law, so the values of Λ_α have to decay exponentially . Thus, a cutoff of such value, will still represent the partition and the state properly. Indeed, for all $\epsilon > 0$, a maximum bond dimension χ can be chosen satisfying:

$$\left\| |\Psi\rangle - \underbrace{\sum_{\alpha=1}^{\chi} \Lambda_\alpha \left|\Phi_\alpha^L\right\rangle \otimes \left|\Phi_\alpha^R\right\rangle}_{|\psi^{\mathrm{trunc}}\rangle} \right\| < \epsilon$$

Additionally, this representation is highly convenient, as the Schmidth coefficients are accesible, while it is expressed in the simple computational base. This makes the computation of local operators extremely efficient 5. Note that local operators only send a given $|i_k\rangle$ to another element $|i_k\rangle$ from the same space. The rest of the indices are not touch, and due to the orthonormalized condition imposed in the construction, identities are automatically recovered.

A.2 MPO

An operator will be represented by the so called *matrix product operator* (MPO).

$$O = \sum_{\substack{j_1,\dots,j_N \\ j'_1,\dots,j'_N}} v^L O^{[1]j_1 j'_1} O^{[2]j_2 j'_2} \dots O^{[N]j_N j'_N} v^R \, |j_1,\dots,j_N\rangle \langle j'_1,\dots,j'_N|$$

Where $O^{[n]j_n j'_n}$ are $d \times d$ matrices and $|j_n\rangle$ represent the local basis of the positions n. The tensor representation is given by Figure 4

A.3 TEBD

As mentioned in the main text, the DMRG is used for local 1D Hamiltonian, which have a gap in the energy spectrum. The fact of only having local interaction, can also be used for the time evolution. The biggest problem to break $U(t)$ into smaller pieces is that the local terms of the Hamiltonian do not neccesarily commute. See for example

$$H = \sigma_1^z \otimes \sigma_2^z + \sigma_2^z \otimes \sigma_3^z$$

where the two terms do not commute.

The better known algorithm that handles this problem is the Time Evolution Block Decimation, which makes used of the Suzuki-Trotter decomposition [Suz91] to break operator $U(t)$ into smaller pieces. It gives the decomposition:

$$e^{(X+Y)\delta} = e^{X\delta} e^{Y\delta} + \mathcal{O}\left(\delta^2\right)$$
$$e^{(X+Y)\delta} = e^{X\delta/2} e^{Y\delta} e^{X\delta/2} + \mathcal{O}\left(\delta^3\right)$$

Indeed, if the interaction terms are only of nearest neighbours, the full Hamiltonian can be broken into two an even and odd Hamiltonians, which do not commute between them, but whose terms commute:

$$H = \underbrace{\sum_{n \text{ odd}} h^{[n,n+1]}}_{H_{\text{odd}}} + \underbrace{\sum_{n \text{ even}} h^{[n,n+1]}}_{H_{\text{even}}}.$$

In this way, using the decomposition, each of $H_{\text{even/odd}}$ can be written as a product of exponent operators as:

$$e^{H_{\text{even/odd}}\delta} = \prod_{n \text{ even/odd}} e^{h^{[n,n+1]}\delta}$$

Which gives the general decomposition of:

$$U(\delta t) \approx \left[\prod_{n \text{ odd}} U^{[n,n+1]}(\delta t)\right] \left[\prod_{n \text{ even}} U^{[n,n+1]}(\delta t)\right],$$

A.4 DMRG

In the DMRG algorithm, only two neighboring sites will be optimized. The state is given by:

$$|\psi\rangle = \sum_{\alpha_n, j_n, j_{n+1}, \alpha_{n+2}} \Theta^{j_n j_{n+1}}_{\alpha_n \alpha_{n+2}} |\alpha_n\rangle_L |j_n\rangle |j_{n+1}\rangle |\alpha_{n+2}\rangle_R .$$

Where $|\psi\rangle_L$ and $|\psi\rangle_R$ are the left and right environments, and the tensor Θ has rank 4 and represents the two neighbouring sites. The upper indices represent the physical legs and the two lower ones the bonds 6:

$$\Theta^{j_n j_{n+1}}_{\alpha_n \alpha_{n+2}} = \sum_{\alpha_{n+1}} \Lambda^{[n]}_{\alpha_n \alpha_n} B^{[n], j_n}_{\alpha_n \alpha_{n+1}} B^{[n+1], j_{n+1}}_{\alpha_{n+1} \alpha_{n+2}}.$$

Now, using the MPO representation of the Hamiltonian, it can be projected into this space contracting the legs that are not in this subspace, i.e. all expect $j_n, j_{n+1}, \alpha_n, \alpha_{n+2}$. This will enable to minimize the energy of this effective Hamiltonian:

$$E = \left\langle \tilde{\psi} \middle| H^{\text{eff}} \middle| \tilde{\psi} \right\rangle,$$

which has dimensions $\chi^2_{\max} d^2 d^2 \chi^2_{\max}$, much smaller than the original one. This process is sketched in Figure 6. For the minimization, a vectorization is first carried out, such that the state becomes a vector and the Hamiltonian a matrix. For the optimization, as the diagonalization might be expensive for large $\chi_{\max}$, any variational algorithms such as Lanczos might be useful. After the minimization, the new bond dimension will have grown to χd. At this point, the renormalization is carried out. First, a SVD is applied, which will decompose the matrix into $\tilde{A}^{[n]}_{\alpha_n \alpha_{n+1}} \tilde{\Lambda}^{[n+1]}_{\alpha_{n+1} \alpha_{n+1}}, \tilde{B}^{[n+1]}_{\alpha_{n+1} \alpha_{n+2}}$. Then, the amount of singular values of $\tilde{\Lambda}^{[n+1]}_{\alpha_{n+1} \alpha_{n+1}}$ will be truncated, such that the maximum bond dimension is respected.

A.5 Transfer matrix

The explicit representation of an infinite MPS would be:

$$|\psi\rangle = \sum_{\ldots j_{n-1}, j_n, j_{n+1}, \ldots} \cdots M^{[n-1] j_{n-1}} M^{[n] j_n} M^{[n+1] j_{n+1}} \cdots |\ldots, j_{n-1}, j_n, j_{n+1}, \ldots\rangle$$

for the symmetry, $M^{[n]} \to M^{[n+L]}$ can be demanded, where the $M^{[n]} M^{[n+1]} \ldots M^{[n+L-1]} M^{[n+L]}$ tensors are repeated after L positions, L being the unit cell length.

The contraction for the *transfer-matrix* is:

$$T_{\alpha\bar{\alpha}, \gamma\bar{\gamma}} = \sum_{j_1, j_2, \beta, \bar{\beta}} M^{[1] j_1}_{\alpha\beta} \overline{M^{[1] j_1}_{\bar{\alpha}\bar{\beta}}} M^{[2] j_2}_{\beta\gamma} \overline{M^{[2] j_2}_{\bar{\beta}\bar{\gamma}}}$$

Where, $\bar{M}$ denotes the complex conjugate. The diagram can be observe in Figure 7 The transfer matrix is the contraction of the states with its conjugate.

This matrix can obviously be written in the canonical form. For that case, the orthonormality condition of the Schmidth vectors translate into eigenvector equations.

When normalizing a vector, the norm is one. As in this case there is a matrix, the matrix must map the identity vector into another identity vector. mathematically:

$$\sum_{\gamma\bar{\gamma}} T_{\alpha\bar{\alpha}, \gamma\bar{\gamma}} \delta_{\gamma\bar{\gamma}} = \delta_{\alpha\bar{\alpha}}$$

$$\sum_{\alpha\bar{\alpha}} \left(\Lambda^{[1]}_{\alpha}\right)^2 \delta_{\alpha\bar{\alpha}} T_{\alpha\bar{\alpha}, \gamma\bar{\gamma}} = \delta_{\gamma\bar{\gamma}}$$

This implies that the largest eigenvalue is normalized to one, so the rest of the eigenvalues must be smaller than one. Thus, the repeated multiplication of this matrix projects any state into the dominant left and right eigenvectors, i.e. the one corresponding to the eigenvalue one.

Taking the espectral decomposition of the transfer matrix:

$$T_{\alpha\bar{\alpha},\gamma\bar{\gamma}} = \delta_{\alpha\bar{\alpha}}\delta_{\bar{\gamma}\bar{\gamma}} + (\eta_2)\,\eta^R_{2,\alpha\bar{\alpha}}\eta^L_{2,\gamma\bar{\gamma}} + (\eta_3)\,\eta^R_{3,\alpha\bar{\alpha}}\eta^L_{3,\gamma\bar{\gamma}} + \dots$$

where $\eta_2, \eta_3, \dots$ represent the eigenvalues and $\eta^R_{2,\alpha\bar{\alpha}}, \eta^R_{3,\alpha\bar{\alpha}}, \dots$ the right and $\eta^L_{2,\alpha\bar{\alpha}}, \eta^L_{3,\alpha\bar{\alpha}}, \dots$ left eigenvectors (Figure 8).

Due to the orthogonalization of the elements, taking the powers of this matrix is straightforward:

$$T^N_{\alpha\bar{\alpha},\gamma\bar{\gamma}} = \delta_{\alpha\bar{\alpha}}\delta_{\bar{\gamma}\bar{\gamma}} + (\eta_2)^N\,\eta^R_{2,\alpha\bar{\alpha}}\eta^L_{2,\gamma\bar{\gamma}} + (\eta_3)^N\,\eta^R_{3,\alpha\bar{\alpha}}\eta^L_{3,\gamma\bar{\gamma}} + \dots$$

The expectation value can then be approximated using just:

$$\langle\psi\,|O_nO_m|\,\psi\rangle = \langle\psi\,|O_n|\,\psi\rangle\,\langle\psi\,|O_m|\,\psi\rangle + (\eta_2)^N\left(O^L_n\eta^R_2\right)\left(\eta^L_2O^R_n\right) + \cdots .$$

where N is the number of unit cells between n and m. O^L_n represent the contraction of the M with the O_n operators. As the terms between the parenthesis is just a number, and the only dependence of the length is $(\eta_2)^N$, we can extract the correlation length as:

$$\langle\Psi|O_nO_m|\Psi\rangle = C\exp\left(\frac{NL}{\xi}\right) \Rightarrow \xi = -\frac{L}{\log|\eta_2|}$$

iDMRG

The general approach to compute states in the thermodynamic limit is to observe how it changes with the size of the system.

In the infinite DMRG [Sch11], the starting point is the unit cell of the iMPS. As with the finite case, the first step is the optimization of two neighboring sites with respect to the local effective Hamiltonian. The subtle change is that the edges also have to be optimized, such that when the unit cells are put next to each other, the edges still represent the bond between two lattice sites $(L, L+1) \equiv (L, 1)$

Once a complete sweep is carried out, an extra unit cell is added to each of sides, which will form part of the environment. As before, a new sweep over the unit cell is carried out, but now the system will be larger and the environments will have the effect of previous optimizations. With each sweep, the environment takes more neighbours into account, so the unit cell starts approaching the thermodynamic limit.

The last important fact about the iDMRG, which is crutial for studying the SSB phases, is that the ground state usually breaks the symmetry of the corresponding phase. This is caused by the broken symmetry of the initial environments added to the edges. With other numerical methods, if the Hamiltonian has a symmetry, this will still be present in the ground state. For those, a pinning Hamiltonian is used for breaking this symmetry [JGP+22]. This can, however, slightly change the state, affecting the results.

iTEBD

For infinite lattices, translational invariance can be exploited to efficiently implement one-dimensional time-evolution simulations [Vid07]. The only requirement is that the Hamiltonian is translationally invariant by L sites. Since applying the operator $e^{ih[n,n+1]}$ also affects positions $[n+L, n+L+1]$, only the time evolution of a single unit cell is necessary.

The primary difference from the finite case, similar to iDMRG, is the additional evolution of the bond $h^{[L,L+1]} \equiv h^{[L,1]}$.

B Optimization of NCM

If $0, s < r, r - s$ is satisfied, notice that there are three blocks for the contractions: the left environment with $c^\dagger_{0,\sigma} c_{s,\sigma}$, the transfer matrix, and $c^\dagger_{s,\sigma'} c_{0,\sigma'}$. In the last one, the r is absorbed in the transfer matrix. This is convenient because larger values of r are easily computed using previous calculations

For the first step, the left environment is contracted with the transfer matrix, and saved in memory. Then, it is contracted with the right environment, giving the first expectation value of the operators with a single transfer matrix in the middle. For the next expectation value, the previous left environment is recovered, contracted with the same transfer matrix again and saved in memory. Finally, it is again contracted with the right environment, giving the expectation value with two transfer matrices in the middle.

To illustrate this procedure, consider the example where $s = 1$. The first computation will give $\left\langle c^\dagger_{0,\sigma} c_{1,\sigma} c^\dagger_{3,\sigma'} c_{2,\sigma'} \right\rangle$, while the second one will move the two tensors in the right two positions, giving $\left\langle c^\dagger_{0,\sigma} c_{1,\sigma} c^\dagger_{5,\sigma'} c_{4,\sigma'} \right\rangle$.

For small systems, this might not be the most efficient method to compute such noise correlators, but it is needed for larger systems, where the number of contractions grows rapidly.

Even if easy to implement for the some values, the case where $0, s < r, r - s$ is not satisfied is problematic, as the transfer matrix cannot be inserted in the middle. For such cases, though, the commutation relations of the creation and annihilation operators can be used. The idea is to arrange the positions such that $0, s < r, r - s$ is satisfied, compute the expectation values efficiently, and go back to the original order.

First, for simplicity, consider that $r \neq s \neq 0$. Those are the cases where two elements of the expectation value are the same, and the operators do not anti-commute. For the general case where spin is different, note that the terms that are not ordered, e.g. $\left\langle c^\dagger_{0,\sigma} c_{2,\sigma} c^\dagger_{3,\sigma'} c_{1,\sigma'} \right\rangle$, can be deduced from the expectation value of $\left\langle c^\dagger_{0,\sigma} c_{1,\sigma'} c^\dagger_{3,\sigma'} c_{2,\sigma} \right\rangle$, where the condition is satisfied. However, the sign has to be recovered:

$$\left\langle c^\dagger_{0,\sigma} c_{2,\sigma} c^\dagger_{3,\sigma'} c_{1,\sigma'} \right\rangle = - \left\langle c^\dagger_{0,\sigma} c_{1,\sigma'} c^\dagger_{3,\sigma'} c_{2,\sigma} \right\rangle . \tag{8}$$

An additional trick comes from, noticing that using the commutation relations and translational symmetry, the negative values of s can also be recovered:

$$\left\langle c^\dagger_{0,\sigma} c_{2,\sigma} c^\dagger_{3,\sigma'} c_{1,\sigma'} \right\rangle = \left\langle c^\dagger_{3,\sigma} c_{1,\sigma} c^\dagger_{0,\sigma'} c_{2,\sigma'} \right\rangle = \left\langle c^\dagger_{1,\sigma} c_{-1,\sigma} c^\dagger_{-2,\sigma'} c_{0,\sigma'} \right\rangle ,$$

which reduced the computation to $s > 0$.

Alternatively, the negative values of r can also be recovered taking the hermitian conjugate of the initial expectation value.

$$\left(\left\langle c^\dagger_{0,\sigma} c_{2,\sigma} c^\dagger_{3,\sigma'} c_{1,\sigma'} \right\rangle \right)^\dagger = \left\langle c^\dagger_{1,\sigma} c_{3,\sigma'} c^\dagger_{2,\sigma'} c_{0,\sigma} \right\rangle = \left\langle c^\dagger_{0,\sigma} c_{2,\sigma} c^\dagger_{3,\sigma'} c_{1,\sigma'} \right\rangle^* .$$

Reducing the computation to $r > 0$.

For the case where the spins are the same, there are still more simplifications. 8 now becomes:

$$\left\langle c^\dagger_{0,\sigma} c_{2,\sigma} c^\dagger_{3,\sigma} c_{1,\sigma} \right\rangle = - \left\langle c^\dagger_{0,\sigma} c_{1,\sigma} c^\dagger_{3,\sigma} c_{2,\sigma} \right\rangle .$$

This is important because now the two terms appear in the original definition of the noise correlator. In that expression, there is a term $e^{id(r-s)}$ multiplying the expectation value. In the next section, it will be shown that the interesting case is that of $d = \pi$, so it becomes $e^{i\pi(r-s)}$. Thus, there are some cases where the two terms cancel out, and they do not need to be computed.

C Thermodynamic limit

The full expression is:

$$
\begin{aligned}
\mathrm{NCM} = &\sum_{\sigma,\sigma'} \Big(\langle \hat{c}^\dagger_{0,\sigma} \hat{c}_{0,\sigma} \hat{c}^\dagger_{100,\sigma'} \hat{c}_{100,\sigma'} \rangle + \langle \hat{c}^\dagger_{1,\sigma} \hat{c}_{1,\sigma} \hat{c}^\dagger_{100,\sigma'} \hat{c}_{100,\sigma'} \rangle \\
&+ \langle \hat{c}^\dagger_{0,\sigma} \hat{c}_{0,\sigma} \hat{c}^\dagger_{101,\sigma'} \hat{c}_{101,\sigma'} \rangle + \langle \hat{c}^\dagger_{1,\sigma} \hat{c}_{1,\sigma} \hat{c}^\dagger_{101,\sigma'} \hat{c}_{101,\sigma'} \rangle \Big) \\
&+ \sum_{\sigma,\sigma'} \Big(\langle \hat{c}^\dagger_{0,\sigma} \hat{c}_{100,\sigma'} \hat{c}^\dagger_{100,\sigma'} \hat{c}_{0,\sigma} \rangle - \langle \hat{c}^\dagger_{0,\sigma} \hat{c}_{101,\sigma'} \hat{c}^\dagger_{101,\sigma'} \hat{c}_{0,\sigma} \rangle \\
&- \langle \hat{c}^\dagger_{1,\sigma} \hat{c}_{100,\sigma'} \hat{c}^\dagger_{100,\sigma'} \hat{c}_{1,\sigma} \rangle + \langle \hat{c}^\dagger_{1,\sigma} \hat{c}_{101,\sigma'} \hat{c}^\dagger_{101,\sigma'} \hat{c}_{1,\sigma} \rangle \Big) \\
&+ (-1)^j \mathrm{Re} \left(\sum_\sigma \langle \hat{c}^\dagger_{0,\sigma} \hat{c}_{j,\sigma} \rangle \cdot \sum_{\sigma'} \langle \hat{c}_{j,\sigma} \hat{c}^\dagger_{0,\sigma} \rangle \right) \times 2 \\
&+ (-1)^j \mathrm{Re} \left(\sum_\sigma \langle \hat{c}^\dagger_{1,\sigma} \hat{c}_{j+1,\sigma} \rangle \cdot \sum_{\sigma'} \langle \hat{c}_{j+1,\sigma} \hat{c}^\dagger_{1,\sigma} \rangle \right) \times 2 \\
&+ (-1)^j \mathrm{Re} \left(\sum_\sigma \langle \hat{c}^\dagger_{0,\sigma} \hat{c}_{j,\sigma} \rangle \cdot \sum_{\sigma'} \langle \hat{c}_{j+1,\sigma} \hat{c}^\dagger_{1,\sigma} \rangle \right) \times 2 \\
&+ (-1)^j \mathrm{Re} \left(\sum_\sigma \langle \hat{c}^\dagger_{1,\sigma} \hat{c}_{j+1,\sigma} \rangle \cdot \sum_{\sigma'} \langle \hat{c}_{j,\sigma} \hat{c}^\dagger_{0,\sigma} \rangle \right) \times 2 \\
&+ (-1)^j \mathrm{Re} \left(- \sum_\sigma \Big(\langle \hat{c}^\dagger_{0,\sigma} \hat{c}_{j,\sigma} \rangle \cdot \langle \hat{c}_{j,\sigma} \hat{c}^\dagger_{0,\sigma} \rangle \Big) \right) \times 2 \\
&+ (-1)^j \mathrm{Re} \left(- \sum_\sigma \Big(\langle \hat{c}^\dagger_{1,\sigma} \hat{c}_{j+1,\sigma} \rangle \cdot \langle \hat{c}_{j+1,\sigma} \hat{c}^\dagger_{1,\sigma} \rangle \Big) \right) \times 2 \\
&+ (-1)^{j-1} \mathrm{Re} \left(- \sum_\sigma \Big(\langle \hat{c}^\dagger_{0,\sigma} \hat{c}_{j,\sigma} \rangle \cdot \langle \hat{c}_{j+1,\sigma} \hat{c}^\dagger_{1,\sigma} \rangle \Big) \right) \times 2 \\
&+ (-1)^{j-1} \mathrm{Re} \left(- \sum_\sigma \Big(\langle \hat{c}^\dagger_{1,\sigma} \hat{c}_{j+1,\sigma} \rangle \cdot \langle \hat{c}_{j,\sigma} \hat{c}^\dagger_{0,\sigma} \rangle \Big) \right) \times 2
\end{aligned}
$$

D Numerical simulations

The numerical sumations were performed using TenPy [HP18]. The iMPS had maximum bond dimension of $\chi = 200$ and the unit cell had length $L = 2$. Ground states were found using iDMRG. No optimization was carried out in the first four sweeps, so the environments broke the symmetry of the ground state. For faster convergence and symmetry breaking, the initial states for $V < 2.4$ where $|\uparrow\downarrow\uparrow\downarrow\rangle$, while for $V > 2.4$ where $|\uparrow\downarrow - \uparrow\downarrow -\rangle$. Particle number N and spin S_z were conserved.

For the time evolution, iTEBD was used. For the truncation, SVD was used, with minimum significant value of 10^{-12}. Fourth order approximation were used, with a time steps of $dt = 0.05$. The computation of the NCM were performed using the reconstruction of a state with 100 particles.

Used parameters for the Hamiltonian were: $t = 1, U = 4, J = 0.5, \Delta = 10$.